

# The Impact of Density Ratio on the Liquid Core Dynamics of a Turbulent Liquid Jet Injected Into a Crossflow

**Marcus Herrmann**  
School for Engineering of Matter, Transport and  
Energy,  
Arizona State University,  
Tempe, AZ 85287  
e-mail: marcus.herrmann@asu.edu

**Marco Arienti**  
**Marios Soteriou**

United Technologies Research Center,  
Hartford, CT 06108

*Atomizing liquids by injecting them into crossflows is a common approach in gas turbines and augmentors. Much of our current understanding of the processes resulting in atomization of the jets, the resulting jet penetration and spray drop size distribution have been obtained by performing laboratory experiments at ambient conditions. Yet, operating conditions under which jets in crossflows atomize can be far different from ambient. Hence, several dimensionless groups have been identified that are believed to determine jet penetration and resulting drop size distribution. These are usually the jet and crossflow Weber and Reynolds numbers and the momentum flux ratio. In this paper, we aim to answer the question of whether an additional dimensionless group, the liquid to gas density ratio must be matched. We perform detailed simulations of the primary atomization region using the refined level set grid (RLSG) method to track the motion of the liquid/gas phase interface. We employ a balanced force, interface projected curvature method to ensure high accuracy of the surface tension forces, use a multiscale approach to transfer broken off, small scale nearly spherical drops into a Lagrangian point particle description allowing for full two-way coupling and continued secondary atomization, and employ a dynamic Smagorinsky large eddy simulation (LES) approach in the single phase regions of the flow to describe turbulence. We present simulation results for a turbulent liquid jet ( $q=6.6$ ,  $We=330$ , and  $Re=14,000$ ) injected into a gaseous crossflow ( $Re=740,000$ ) analyzed under ambient conditions (density ratio 816) experimentally by Brown and McDonnell [2006, "Near Field Behavior of a Liquid Jet in a Crossflow," Proceedings of the ILASS Americas, 19th Annual Conference on Liquid Atomization and Spray Systems]. We compare simulation results obtained using a liquid to gas density ratio of 10 and 100. The results show that the increase in density ratio causes a noticeable increase in liquid core penetration with reduced bending and spreading in the transverse directions. The post-primary atomization spray penetrates further in both the jet and transverse direction. Results further show that the penetration correlations for the windward side trajectory commonly reported in the literature strongly depend on the value of threshold probability used to identify the leading edge. Correlations based on penetration of the jet's liquid core center of mass, on the other hand, can provide a less ambiguous measure of jet penetration. Finally, the increase in density ratio results in a decrease in wavelength of the most dominant feature associated with a traveling wave along the jet as determined by proper orthogonal decomposition.*

[DOI: 10.1115/1.4002273]

## 1 Introduction

The atomization of turbulent liquid jets injected into fast moving, subsonic gaseous crossflows is an important application, for example, in gas turbines, ramjets, and augmentors. It is a highly complex process that has been extensively studied experimentally over the past decades. Early studies of the atomization of nonturbulent liquid jets in crossflows were recently reviewed in Ref. [1], whereas newer studies of this case include the work reported in Refs. [2–12]. Most experimental work has focused on jet penetration, including both the column trajectory and the resulting spray penetration under ambient, atmospheric conditions. Some recent jet penetration correlations under these conditions can be found in Refs. [3,10–12]. Under nonatmospheric conditions, jet penetration correlations were derived in Refs. [2,13,14]. The identified char-

acteristic parameters determining jet penetration from these studies are summarized in Table 1. Since gaseous density is proportional to channel pressure, only the correlations in Refs. [13,14] contained the impact of density ratio on liquid jet penetration directly, reporting a slight decrease in penetration with decreased density ratio. However, although momentum flux ratio and crossflow and jet Weber numbers were approximately held constant, at least one of the Reynolds numbers could not have been maintained, thus, potentially overlapping two separate effects. It should be pointed out that some other studies exist that vary the channel pressure from its atmospheric value, however, these studies consider modified configurations, for example, airblast assisted atomization [15], or did not result in modifications to the liquid jet core penetration correlations [16].

Unlike most experimental studies, detailed numerical simulations of turbulent atomization processes are typically performed at density ratios smaller than those found in gas turbine combustors due to often times encountered numerical instabilities associated with the density discontinuity on highly deformed interfaces. The

Contributed by the International Gas Turbine Institute (IGTI) of ASME for publication in the JOURNAL OF ENGINEERING FOR GAS TURBINES AND POWER. Manuscript received May 30, 2010; final manuscript received May 31, 2010; published online February 15, 2011. Editor: Dilip R. Ballal.

**Table 1 Parameters impacting jet penetration**

	$q$	$We_c$	$\frac{\mu_{H_2O}}{\mu_l}$	$Re_c$	$P_c$
Wu et al. [12]	X				
Thawley et al. [11]	X	X			
Birouk et al. [3]	X		X		
Stenzler et al. [10]	X	X	X		
Bellofiore et al. [2]	X	X		X	
Elshamy and Jeng [13] and Elshamy [14]	X	X			X

question we thus aim to address in this paper is how representative are those simulations at lower density ratio conditions of the actual application.

Besides jet penetration, a change in density ratio while maintaining all other characteristic numbers, might also impact the atomization mechanism of the jet and thus, the breakup length. The experimental data analyzed in Refs. [7,12] suggested that the breakup location in the jet direction is a function of momentum flux ratio only, whereas the location in the crossflow direction is constant. Data analyzed by Bellofiore et al. [2], however, stated that the breakup point in the crossflow direction is a function of crossflow Weber number and the breakup point in the jet direction is a function of momentum flux ratio and crossflow Reynolds number. None of the correlations contain an explicit density ratio dependence.

Finally, Refs. [13,14] reported that spray coverage area is reduced when decreasing the density ratio and Bellofiore et al. [2] observed that the spray extended and the plume width depended not only on the crossflow Weber number but also increased with the square root of the density ratio. Their data contained, however, significant scatter, making the exact dependency on density ratio difficult to ascertain.

The purpose of this paper is to ascertain the importance of density ratio on the atomization process of liquid jets in crossflows, if all characteristic numbers, i.e., momentum flux ratio, crossflow and jet Weber numbers, and crossflow and jet Reynolds numbers are kept constant. We perform detailed simulations of the primary atomization region of a turbulent liquid jet injected into a subsonic gaseous crossflow using the refined level set grid method [17–19]. The operating conditions are for an atomization case analyzed experimentally in Ref. [4]:  $q=6.6$ ,  $We_c=330$ ,  $Re_j=14,000$ , and  $Re_c=570,000$ . We compare simulation results obtained for two different density ratios  $R=10$ , a value used in the past for detailed numerical simulations [18,20], and 100, a value typical of gas turbine combustor injectors.

The outline of this paper is the following. After summarizing the governing equations, the numerical methods employed to solve them are briefly outlined. Then, simulation results are presented and the impact of density ratio on the atomization process is discussed.

## 2 Governing Equations

The motion of an unsteady, incompressible, immiscible, two-fluid system is governed by the Navier–Stokes equations

$$\frac{\partial u}{\partial t} + u \cdot \nabla u = -\frac{1}{\rho} \nabla p + \frac{1}{\rho} \nabla \cdot (\mu(\nabla u + \nabla^T u)) + \frac{1}{\rho} T_\sigma \quad (1)$$

where  $T_\sigma$  is nonzero only at the location of the phase interface  $x_f$ . Furthermore, the continuity equation results in a divergence-free constraint on the velocity field  $\nabla \cdot u=0$ . The phase interface location  $x_f$  between the two fluids is described by a level set scalar  $G$  with  $G(x_f, t)=0$  at the interface  $G(x, t)>0$  in fluid 1 and  $G(x, t)<0$  in fluid 2. Differentiating this with respect to time yields

$$\frac{\partial G}{\partial t} + u \cdot \nabla G = 0 \quad (2)$$

Assuming material properties to be constant within each fluid, they can be calculated from

$$\beta(x) = H(G)\beta_1 + (1 - H(G))\beta_2 \quad (3)$$

where  $\beta$  is either  $\rho$  or  $\mu$ , indices 1 and 2 denote values in fluids 1 and 2, respectively, and  $H$  is the Heaviside function. The surface tension force  $T_\sigma$  can be expressed as

$$T_\sigma(x) = \sigma \kappa \delta(x - x_f) n = \sigma \kappa \delta(G) |\nabla G| n \quad (4)$$

## 3 Numerical Methods

In this section, we first briefly summarize the RLSG method used to track the phase interface during primary atomization. Then, the level set-based balanced force algorithm is reviewed that allows for the accurate and stable treatment of surface tension forces. Finally, the coupling procedure of the RLSG tracked phase interface to the Lagrangian point particle method is described.

**3.1 Refined Level Set Grid Method.** In the RLSG method, all level set-related equations are evaluated on a separate, equidistant Cartesian grid using a dual-narrow band methodology for efficiency. This so-called  $G$ -grid is overlaid onto the flow solver grid on which the Navier–Stokes equations are solved and can be independently refined, providing high resolution of the tracked phase interface geometry. Details of the method, i.e., narrow band generation, level set transport, re-initialization, curvature evaluation, as well as its performance compared with other interface tracking methods in generic advection test cases can be found in Ref. [17].

In the current simulations, refinement of the  $G$ -grid is limited to a factor two in each spatial direction as compared with the flow solver grid. While higher refinements are feasible from an efficiency standpoint, they would require the use of a subflow solver-grid model to correctly capture the otherwise nonresolved phase interface dynamics on the  $G$ -grid scale [21]. Instead, here, the refined  $G$ -grid simply serves to increase the accuracy of the level set-based phase interface tracking scheme.

**3.2 Balanced Force Algorithm.** In the Navier–Stokes equations, the position of the phase interface influences two different terms. The first term is due to Eq. (3) since  $H(G)$  is a function of the position of the phase interface. For finite volume formulations, the volume fraction  $\psi_{cv}$  is defined as

$$\psi_{cv} = 1/V_{cv} \int_{V_{cv}} H(G) dV \quad (5)$$

In the RLSG method, the above integral is evaluated using the high-resolution  $G$ -grid, see Ref. [17] for a detailed description. Then both control volume density and viscosity can be calculated from

$$\beta_{cv} = \psi_{cv}\beta_1 + (1 - \psi_{cv})\beta_2 \quad (6)$$

The second term that is a function of the interface position is the surface tension force term (4). Here, it is critical for stability and accuracy that the surface tension force can be balanced by the pressure gradient (jump) across the phase interface exactly on the discrete level. This is ensured by the balanced force approach [17,22] based on the continuum surface force (CSF) model [23]. Then the surface tension force at the control volume face  $f$  is

$$T_{\sigma_f} = \sigma \kappa_f (\nabla \psi)_f \quad (7)$$

with the phase interface curvature at the control volume face

$$\kappa_f = \frac{\alpha_{cv} \kappa_{cv} + \alpha_{nbr} \kappa_{nbr}}{\alpha_{cv} + \alpha_{nbr}} \quad (8)$$

where nbr is the control volume sharing the face with  $cv$  and

$$\alpha_{cv} = \begin{cases} 1: & 0 < \psi_{cv} < 1 \\ 0: & \text{otherwise} \end{cases} \quad (9)$$

The control volume curvature  $\kappa_{cv}$  is calculated from the phase interface geometry on the high-resolution  $G$ -grid using a second-order accurate interface projected curvature calculation method [17]. A detailed description of the balanced force algorithm for the RLSG level set method and its performance compared with alternative numerical methods in a range of test cases involving capillary forces can be found in Ref. [17].

**3.3 Coupling to Lagrangian Spray Model.** Atomization typically produces a vast number of both large and small scale drops. Resolving the geometry by tracking, the phase interface associated with each of the resulting drops quickly becomes prohibitively expensive. Instead, we follow a multiscale coupled Eulerian/Lagrangian procedure in that we track the phase interface by a Eulerian level set method in the near-injector primary atomization region and transfer broken off, nearly spherical liquid structures into a Lagrangian point particle description. Details of the transfer procedure were described in Ref. [19]. In the Lagrangian description, full two-way momentum coupling between the drop and continuous phase is used, including a stochastic secondary atomization model [24]. However, the cell volume occupied by the Lagrangian drops is not explicitly taken into account and neither the drop/drop nor the drop/tracked phase interface collisions are modeled. But, as long as liquid structures have not been transferred into the Lagrangian description, i.e., they are still tracked by the level set scalar, secondary breakup, cell volume effects, and all collisions are fully captured.

**3.4 Employed Solvers.** In this work, we use the flow solver CDP/CHARLES that solves the incompressible two-phase Navier–Stokes equations on unstructured grids using the finite volume balanced force algorithm [17]. In the single phase regions, the employed scheme conserves the kinetic energy discretely. Turbulence in the single phase regions of the flow is modeled using a dynamic Smagorinsky LES model, however, none of the terms arising from filtering the phase interface are modeled, thus, neglecting the subfilter contributions of the surface tension force and the transport of the phase interface by subfilter velocity fluctuations [21]. To limit the impact of this simplification, we refine the grid in the vicinity of the phase interface significantly, thereby, reducing the magnitude of the neglected terms. Ideally, with fine enough grid resolution at the phase interface, this approach resolves the influence of surface tension on the motion of the phase interface both in terms of initiating surface deformation via the Rayleigh instability mechanism and suppressing surface corrugations due to subgrid eddies. A Lagrangian particle/parcel technique is employed to model the small scale liquid drops of the atomizing liquid spray [25].

The liquid/gas phase interface during primary atomization is tracked by the interface tracking software LIT, using the RLSG method [17]. The solver uses a fifth-order weighted essentially nonoscillatory (WENO) scheme [26] in conjunction with a third-

**Table 2 Operating conditions and characteristic numbers**

	Exp.	Sim. 1	Sim. 2
$D$ (mm)	1.3	1.3	1.3
$\rho_c$ (kg/m <sup>3</sup> )	1.225	1.225	1.225
$\rho_f$ (kg/m <sup>3</sup> )	1000	12.25	122.25
$u_c$ (m/s)	120.4	120.4	120.4
$u_j$ (m/s)	10.83	97.84	30.94
$\mu_c$ (kg/ms)	$1.82 \times 10^{-5}$	$1.82 \times 10^{-5}$	$1.82 \times 10^{-5}$
$\mu_j$ (kg/ms)	$1.0 \times 10^{-3}$	$1.11 \times 10^{-4}$	$3.5 \times 10^{-4}$
$\sigma$ (N/m)	0.07	0.07	0.07
$R$	816	10	100
$q$	6.6	6.6	6.6
$We_c$	330	330	330
$We_j$	2178	2178	2178
$Re_c$	$5.7 \times 10^5$	$5.7 \times 10^5$	$5.7 \times 10^5$
$Re_j$	14,079	14,079	14,079

order total variation diminishing (TVD) Runge–Kutta time discretization [27]. The phase interface's curvature on the level set grid is evaluated using a second-order accurate interface projection method [17].

The flow solver CDP/CHARLES and the interface tracking software LIT are coupled using the parallel multicode coupling library CHIMPS [17,28]. In order to couple the level set equation to the Navier–Stokes equation,  $u$  in Eq. (2) is calculated from the flow solver velocity by trilinear interpolation. To achieve overall second-order accuracy in time, the level set equation is solved staggered in time with respect to the Navier–Stokes equations.

#### 4 Computational Domain and Operating Conditions

The case analyzed in this paper is one studied experimentally by Brown and McDonell [4]. Table 2 summarizes the operating conditions and resulting characteristic numbers for the experiment and the two numerical simulations. Results obtained for the density ratio 10 case were reported previously in Refs. [18,20].

Figure 1 depicts the computational domain and the used boundary conditions as well as a zoom into the near-injector region to show the mesh detail used in the simulations. The chosen computational domain ( $-25D, \dots, 50D \times 0D, \dots, 25D \times -10D, \dots, 10D$ ) is smaller than the channel used in the experiment ( $-77D, \dots, 127D \times 0D, \dots, 54D \times -27D, \dots, 27D$ ). However, simulations using the full experimental channel geometry were conducted to verify that the reduced computational domain does not impact the reported results [29]. Furthermore, in the simulations, the detail of the injector geometry are taken into account, see Refs. [18,20] for further details.

In Refs. [18,20], we reported on a grid refinement study for the  $R=10$  case using three different grid resolutions. The obtained results indicate that jet penetration can be well predicted even on the coarsest grid, column and surface breakup modes can be observed on all three grids, and that grid independent drops resulting from primary atomization can be obtained for drops resolved by at least two grid nodes of the RLSG grid.

Thus, in the following, we will limit ourselves to only one grid resolution, the medium resolution grid c12 used in Refs [18,20]. It

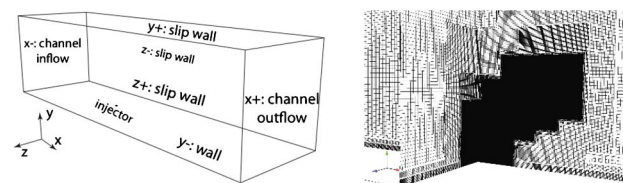


**Fig. 1 Computational domain and boundary conditions (left) and mesh detail near the injector (right)**

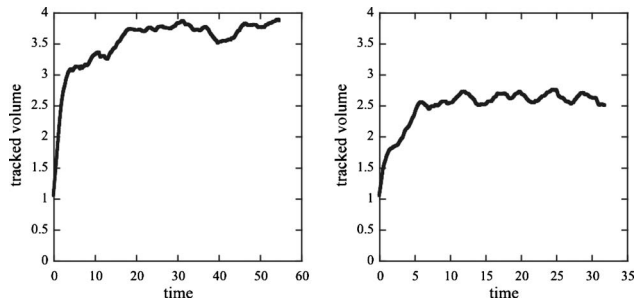


**Fig. 2 Evolution of tracked liquid volume:  $R=10$  (left) and  $R=100$  (right)**

resolves the injector diameter by 32 control volumes in the flow solver and 64 grid nodes in the RLSG solver. The resulting mesh sizes are  $21 \times 10^6$  control volumes for the flow solver and  $13 \times 10^6$  active RLSG grid nodes. At  $t=0$ , the liquid jet is initialized in the computational domain by a small cylindrical section of length  $D$  capped by a half-sphere, protruding into the crossflow channel.

In the following, results are reported in dimensionless quantities, with  $u_j$  and  $D$  being the reference velocity and length. Thus, nondimensional coordinates are the same in both density cases, whereas reference times  $t_{ref}=D/u_j$  are different with one nondimensional time unit representing  $13.3 \mu s$  for  $R=10$  and  $42.5 \mu s$  for  $R=100$ .

## 5 Results and Discussion

Figure 2 shows the temporal evolution of the level set tracked liquid volume for the two different density ratio cases. Both show an initial linear increase. This is due to the fact that at this early stage, almost no small scale drops are generated that would be transferred out of the tracked and into the Lagrangian representation. Then at around  $t=5$  in the  $R=10$  case and  $t=2$  in the  $R=100$  case, significant numbers of small scale drops are generated and transferred from the level set to the Lagrangian representation, resulting in a slower increase in the level set tracked volume until at around  $t=20$  in the  $R=10$  case and  $t=10$  in the  $R=100$  case a statistically steady state is reached. From this point on, a balance exists between the injected liquid mass and the atomized liquid mass that is transferred into the Lagrangian description. Comparing instantaneous snapshots of the surface geometry of the two cases presented in Figs. 3–5, jet penetration appears different with the higher density case being less bent in the crossflow direction and the liquid core not extending as far in that direction. Also, the liquid core appears more compact in the top and front views while the resulting spray drops show significantly more penetration in the jet direction and spread in the transverse direction. This observation is consistent with experimental data reported in Refs. [2,13,14].

To quantify the potential difference, one can look at the mean jet penetration. In experiments, the mean jet penetration is often determined by taking side view shadowgraphy or Mie-scattering pictures of the atomizing jet. Then these images are either first averaged and then thresholded to identify the jet/spray boundary [5,10,30], or the individual images are first thresholded and the resulting jet/spray boundary fits or jet coordinates are then averaged [2,3,11]. The threshold value used to identify the jet/spray boundary in either case can range anywhere from 3% [10,30] of the maximum image intensity or two standard deviations above the mean background noise image intensity [11] to 50% of the local image line maximum intensity [4,5].

Following a procedure similar to the one used in Refs. [5,30], Fig. 6 shows the average of the side view of the atomizing jet of which some snapshots are shown in Fig. 3. No thresholding was applied to either the individual or the averaged images. Averaging

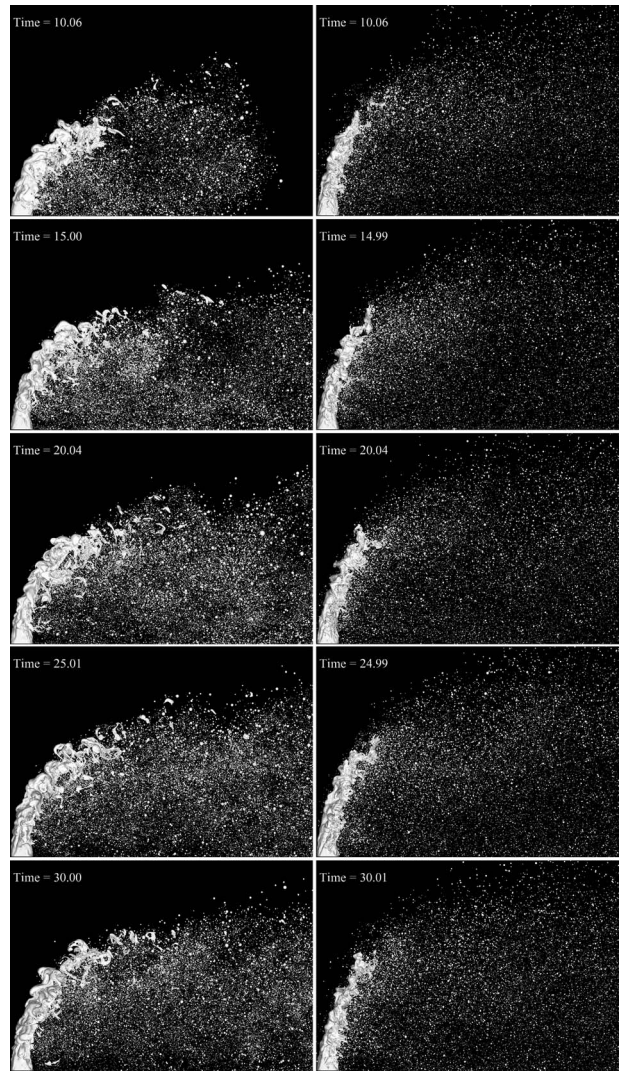


**Fig. 3 Side view snapshots of jet in crossflow atomization at  $t=10, 15, 20, 25,$  and  $30$  time units (top to bottom),  $R=10$  (left), and  $R=100$  (right)**

was done only for images taken after the jet has reached steady state, i.e., for  $t > 20$  in the low density ratio case (for a total of 35 time units) and  $t > 10$  in the high density ratio case (for a total of 22 time units).

The side view jet penetration is compared with the predictions of two common correlations for the penetration of the upper edge of the liquid jet derived by fitting experimental data, namely,

$$\frac{y}{D} = 1.37 \left( q \frac{x}{D} \right)^{1/2} \quad (10)$$

due to Wu et al. [12] valid in the near-injector region only and

$$\frac{y}{D} = 2.63 q^{0.442} \left( \frac{x}{D} \right)^{0.391} \text{We}^{-0.088} \left( \frac{\mu_l}{\mu_{H_2O}} \right)^{-0.027} \quad (11)$$

due to Stenzler et al. [30]. It appears that the agreement with the experiment in the higher density ratio case is better with the Wu et al. correlation [12], which was specifically designed for the near-injector region. However, the comparison is somewhat qualitative.

To allow for a detailed quantitative analysis of the mean jet penetration, we developed a new post-processing tool to extract such data from time snapshots of the level set solution field. Since the interest here is on time averaged data, it should be pointed out that a simple time averaging of the level set scalar is doomed to

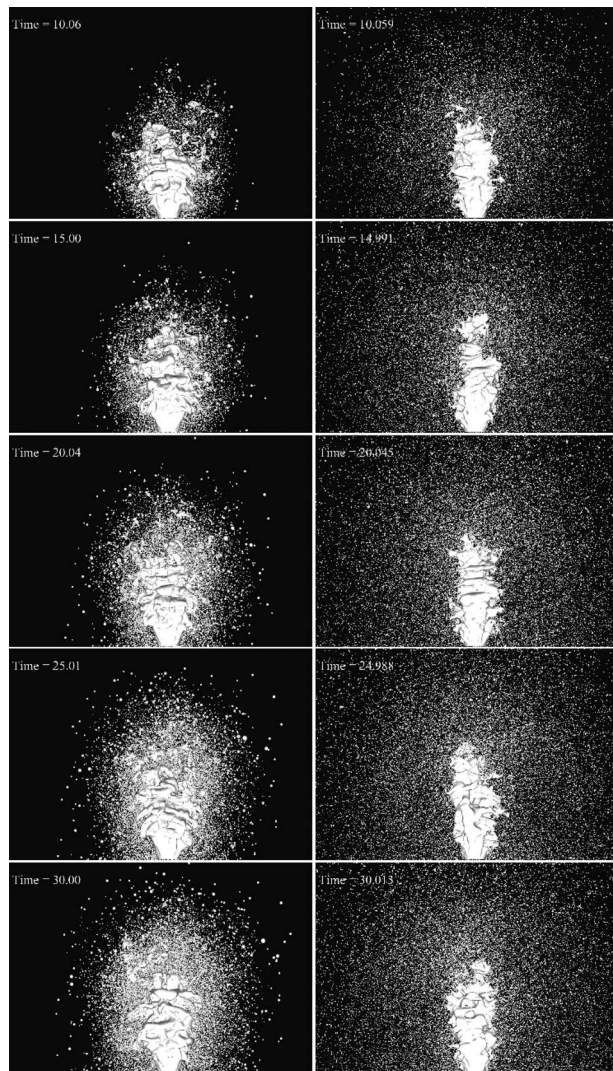


**Fig. 4** Front view snapshots of jet in crossflow atomization at  $t=10, 15, 20, 25,$  and  $30$  time units (top to bottom),  $R=10$  (left), and  $R=100$  (right)

fail and give inaccurate results since such an approach violates the inherent symmetries of the level set equation [31]. Instead, we base our averaging tool on the spatial filters for level set scalars proposed in Ref. [32] applied to temporal filtering instead of spatial filtering. The idea in this approach is to perform the averaging on a Heaviside transform of the level set scalar instead of on the level set scalar itself. This, in essence, results in a scalar that describes the threshold probability of finding liquid at a given location (the probability is  $x\%$  or greater). Additionally, this scalar is consistent with a mean liquid volume fraction. In principle, any value of the resulting scalar can be used to identify the position of the mean surface. A natural choice would be the 50% probability isosurface but any other value can be used as well. Figure 7 shows the probability isosurfaces of 10% and 50% of finding the liquid core for the two density ratios. The lower density ratio case exhibits significantly more expansion in the transverse direction, whereas, the higher density ratio results in a more upright, compact liquid core. This observation is supported by Fig. 8, which presents the position of the liquid core's center of mass and windward and lee-side 50% probability isolines in the injector's center plane. The center of mass position was determined by an iterative procedure evaluating the center of mass in planes normal to its trajectory. Also shown are power law fits, where  $y/D$

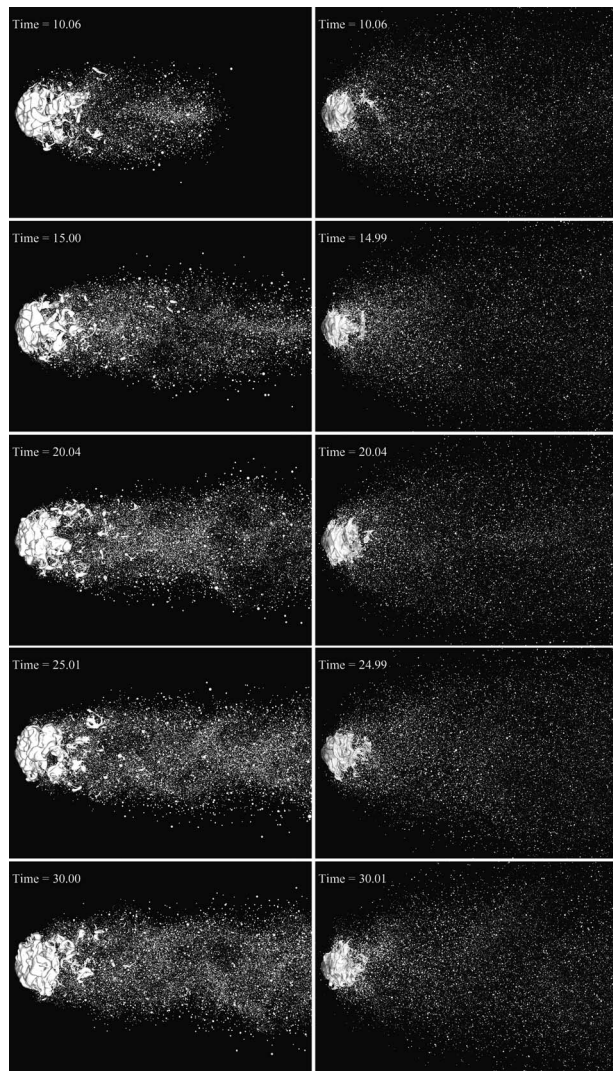


**Fig. 5** Top view snapshots of jet in crossflow atomization at  $t=10, 15, 20, 25,$  and  $30$  time units (top to bottom),  $R=10$  (left), and  $R=100$  (right)

$=3.3(x/D)^{0.33}$  and  $y/D=3.8(x/D)^{0.40}$  fit the center of mass trajectory in the low density and high density ratio case, respectively. The 50% probability leading edge can be fitted by  $y/D=3.18(x/D)^{0.49}$  and  $y/D=3.4(x/D)^{0.45}$ , respectively. The power law fits obtained from experiments are  $y/D=3.5(x/D)^{0.50}$  [12] and  $y/D=3.6(x/D)^{0.39}$  [30].

It should be pointed out that the prefactor and exponent in the power law fit are very sensitive to the chosen value of the prob-

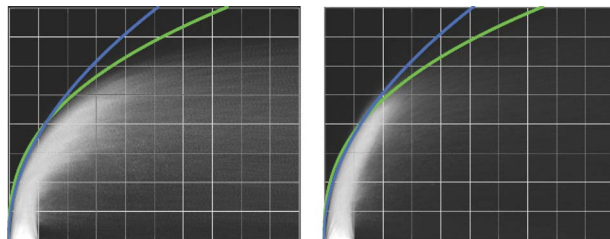


**Fig. 6** Averaged side view of the liquid jet,  $R=10$  (left) and  $R=100$  (right). Jet penetration is compared with liquid jet penetration correlations due to Wu et al. [12] (upper curve) and Stenzler et al. [30] (lower curve).

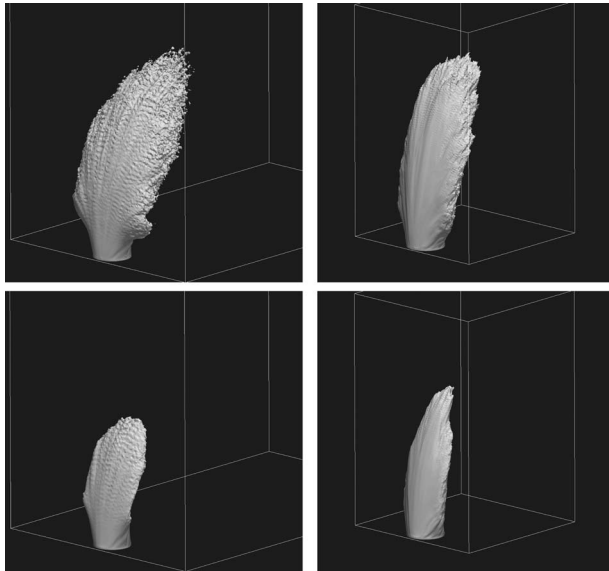


Fig. 7 Impact of density ratio on liquid probability threshold, 10% (top) and 50% (bottom) for  $R=10$  (left) and  $R=100$  (right)

ability isoline. Figure 9 shows the amount of variation in the windward side trajectory obtainable by simply choosing different isovalues, resulting in power law fit prefactors ranging from 2.74 to 3.50 and exponents from 0.39 to 0.52 in the low density case and from 3.1 to 3.7 with exponents from 0.36 to 0.48 in the high density case. This significant spread in parameters highlights a potential weakness in the way windward edge trajectories, and therefore, jet penetration is experimentally measured. The results indicate that the power law parameters are a strong function of the

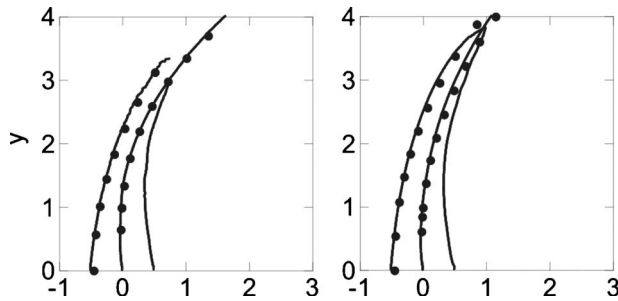


Fig. 8 Impact of density ratio on center of mass (black) and windward and lee side 50% probability isoline in the injector midplane. Symbols are power law fits.  $R=10$  (left) and  $R=100$  (right)

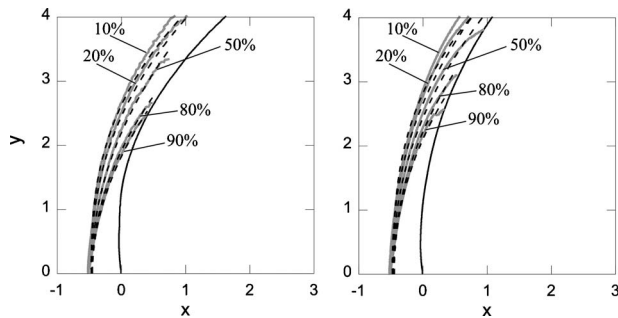


Fig. 9 Impact of probability isovalue on windward edge trajectory, isoline (gray line), and fit (dashed).  $R=10$  (left) and  $R=100$  (right)

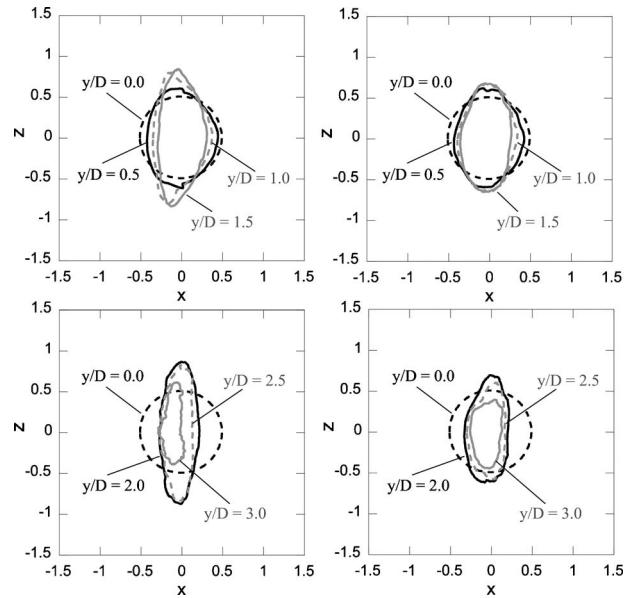


Fig. 10 50% probability surface for  $R=10$  (left) and  $R=100$  (right)

threshold value used to identify the windward edge. A more objective measure for jet penetration would be the jet's center of mass, which is, however, hard to measure experimentally.

Figures 10 and 11 show the 50% and 20% probability isolines of finding liquid in different cut planes normal to the jet's center

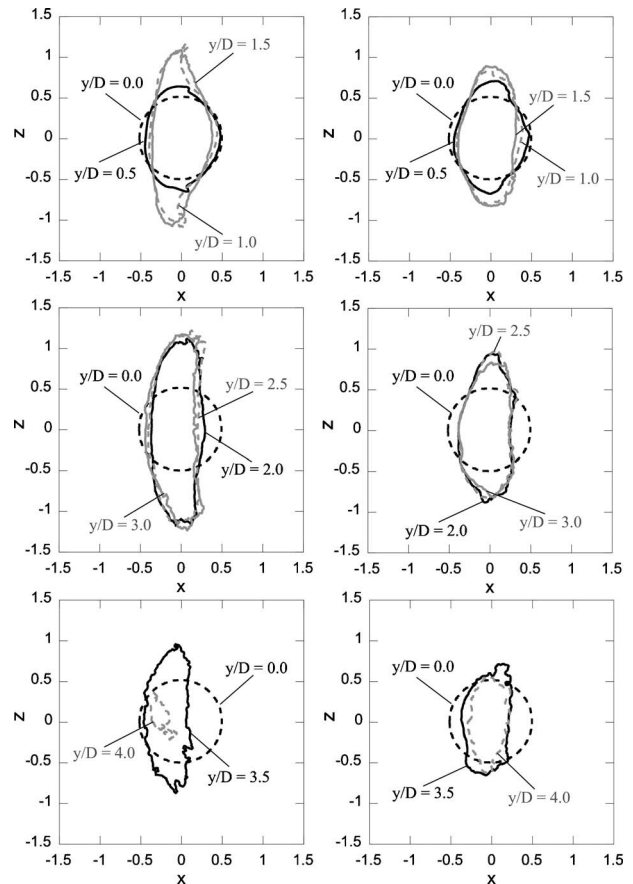


Fig. 11 20% probability surface for  $R=10$  (left) and  $R=100$  (right)

of mass trajectory at varying heights above the injector exit. The origin in these plots corresponds to the jet's center of mass. It has been hypothesized in the recent past that a nonturbulent liquid jet in a uniform crossflow deforms and breaks similarly to the secondary breakup of drops subjected to shock wave disturbances [8,12,33]. Simulation results based on this premise were reported in Ref. [1]. Our simulation results show that the lower density ratio case leads to a quick deformation of the initially circular cross section at the injector exit. After an initial triangular or mode 3 type deformation, the jet's 50% probability line exhibits an almost symmetric elliptical shape. Analyzing the 20% isolines, the jet near the exit shows a small deformation on the sides, reminiscent of a drop stripping mode. Starting at  $y/D=2.0$ , the jet shows a deformation characteristic of drops subjected to crossflows.

In the higher density ratio case, the jet is prone to much less deformation. The 50% isolines do not show a clear initial trend to a mode 3 deformation and the elliptical deformation is much less pronounced at larger distances from the injector exit. This trend of "less deformation" is also clearly evident in the 20% isolines. This shows no bending of the profiles in the crossflow direction near the jet's sides as observed in the low density ratio case. This result is in disagreement with the model results reported in Ref. [1]. There, an increase in density ratio results in an increase in deformation, which is contrary to our observation. This seeming discrepancy might be due to the difference in Weber numbers used,  $We=4$  [1] vs  $We=330$  used here, or due to the presence of turbulence and/or three-dimensional effects.

To study the dynamics of the jet, proper orthogonal modes are generated from side view pictures, see Fig. 3, and ordered by variation of light intensity relative to the time average, Fig. 6. The information in each snapshot is translated into pixel intensity in a range from 0 to 255. The orthogonal decomposition is then carried out through the method of snapshots [34]. The distance between any two snapshots in a sequence of  $N$  observations is defined as their inner product, that is, the pixel by pixel sum of the product of the pixel intensities. The resulting  $N$  by  $N$  spatial correlation matrix is diagonalized to generate a set of basis functions that spans the collection. The first  $M < N$  modes are optimal among all possible truncations of the same order, in the sense that they capture the maximum amount of pixel intensity variation with respect to the time average. An image at time  $t_i$  is reconstructed as

$$z_i = \sum_{r=0}^M a_{r,i} \phi_r \quad (12)$$

Specific features of the dynamics of the jet can be identified by analysis in the frequency domain of the temporal coefficients  $a_{r,i}$  from the orthogonal decomposition, as shown in Ref. [35]. Particularly, features moving along the jet can be found by recalling that a traveling wave is the superposition of two standing waves with half a wavelength delay, the same frequency, and a phase difference of  $\pm 90$  deg. For the  $R=10$  case, Fig. 12 shows two orthogonal modes with similar patterns and well-defined matching peaks of power spectrum density. The wavelength of the associated jet features can be extracted directly from the two modes. The resulting nondimensional wavelength in the low density ratio case is  $\lambda_{10}=1.7$  and in the high density ratio case is  $\lambda_{100}=1.1$ . The dominant frequency at which these features appear can be identified from the cross-power spectrum density between the two time series [35]. Where the amplitude of the correlation density peaks, the phase is approximately of  $\pm 90$  deg. This is shown in Fig. 13 for the two density ratio cases in exam. The dominant frequencies are  $f_{10}=851$  Hz and  $f_{100}=1230$  Hz.

At first glance, it would appear that the observed decrease in wavelength with increasing density ratio and decreasing jet velocity, see Table 2, would rule out the Kelvin–Helmholtz instability as the driving mechanism for the observed waves since the classical theory would predict an increase in wavelength [36]. However, such a simplified analysis would neglect several important

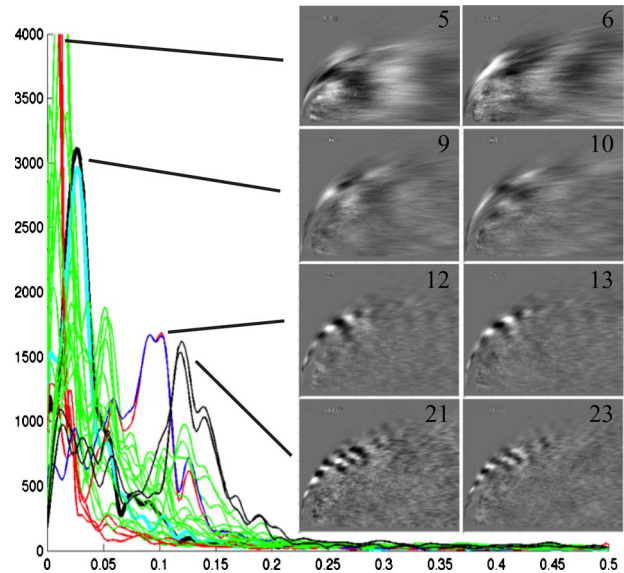


Fig. 12 Proper orthogonal decomposition for  $R=10$ . Shown on the left from top left to bottom right are modes 5, 6, 9, 10, 12, 13, 21, and 23.

contributions, among them the presence of competing viscous modes and the structure of the liquid and gaseous boundary layer profiles [37,38], as well as the impact of the deflected gaseous crossflow and the fact that quantities are varying along the jet's

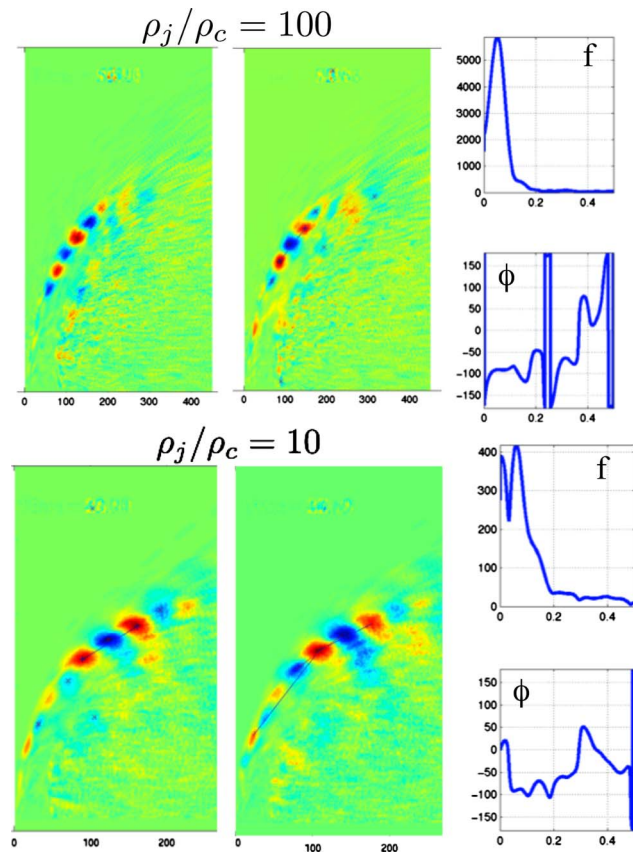


Fig. 13 Proper orthogonal decomposition for  $R=10$  (bottom) and  $R=100$  (top). Shown on the right are frequency  $f$  and phase  $\phi$ .

path. The necessary detailed analysis is beyond the scope of the current paper but will be addressed in future work.

## 6 Conclusion

Detailed simulation results of the primary atomization of a turbulent liquid jet injected into a subsonic gaseous crossflow previously analyzed experimentally in Ref. [4] have been presented, studying the impact of density ratio on the primary atomization region. The simulation results indicate that the density ratio has a noticeable effect on the primary atomization region, even if all other relevant characteristic numbers are being kept constant. An increase in density ratio results in a noticeable increase in liquid core penetration with reduced bending in the crossflow and spreading in the transverse directions. The post-primary atomization spray, however, penetrates further in both the jet and transverse direction. Results further show that penetration correlations for the windward side trajectory commonly reported in the literature strongly depend on the value of threshold probability used to identify the leading edge. Correlations based on the penetration of the jet's liquid core center of mass, on the other hand, can provide a less ambiguous measure of jet penetration. Finally, the increase in density ratio results in a decrease in wavelength of the most dominant feature associated with a traveling wave along the jet as determined by proper orthogonal decomposition.

It should be pointed out, however, that these conclusions are drawn using the exact same fixed grid resolution in both cases. While grid refinement studies performed for the low density case indicate that jet penetration is grid independent for the employed grid [18,20], it is hypothesized, albeit not proven, that this same standard applies to the high density ratio case.

## Acknowledgment

This work was supported in part by CASCADE Technologies, Inc., under the NavAir Contract No. SBIR N07-046.

## Nomenclature

$D$	= jet exit diameter
$\delta$	= delta function
$G$	= level set scalar
$H$	= Heaviside function
$\kappa$	= interface curvature
$\mu$	= dynamic viscosity
$n$	= interface normal vector
$p$	= pressure
$\Psi$	= volume fraction
$q$	= momentum flux ratio
$R$	= density ratio, $R = \rho_j / \rho_c$
Re	= Reynolds number
$\rho$	= density
$\sigma$	= surface tension coefficient
$t$	= time
$T_\sigma$	= surface tension force
$u$	= velocity
$V$	= volume
We	= Weber number
$x$	= cross flow direction
$x_f$	= interface location
$y$	= jet direction

## Subscripts

$c$	= crossflow
$cv$	= control volume
$f$	= control volume face
$j$	= jet
$l$	= liquid

## References

- [1] Aalburg, C., van Leer, B., Faeth, G. M., and Sallam, K. A., 2005, "Properties

- of Nonturbulent Round Liquid Jets in Uniform Gaseous Cross Flows," *Atomization Sprays*, **15**(3), pp. 271–294.
- [2] Bellofiore, A., Cavaliere, A., and Ragucci, R., 2007, "Air Density Effect on the Atomization of Liquid Jets in Crossflow," *Combust. Sci. Technol.*, **179**(1–2), pp. 319–342.
- [3] Birouk, M., Iyogun, C. O., and Popplewell, N., 2007, "Role of Viscosity on Trajectory of Liquid Jets in a Cross-Airflow," *Atomization Sprays*, **17**(3), pp. 267–287.
- [4] Brown, C. T., and McDonell, V. G., 2006, "Near Field Behavior of a Liquid Jet in a Crossflow," *Proceedings of the ILASS Americas, 19th Annual Conference on Liquid Atomization and Spray Systems*.
- [5] Brown, C. T., Mondragon, U. M., and McDonell, V. G., 2007, "Investigation of the Effect of Injector Discharge Coefficient on Penetration of a Plain Liquid Jet Into a Subsonic Crossflow," *Proceedings of the ILASS Americas 20th Annual Conference on Liquid Atomization and Spray Systems*.
- [6] Fuller, R. P., Wu, P.-K., Kirkendall, K. A., and Nejad, A. S., 2000, "Effects of Injection Angle on Atomization of Liquid Jets in Transverse Airflow," *AIAA J.*, **38**(1), pp. 64–72.
- [7] Lee, K., Aalburg, C., Diez, F. J., Faeth, G. M., and Sallam, K. A., 2007, "Primary Breakup of Turbulent Round Liquid Jets in Uniform Crossflows," *AIAA J.*, **45**(8), pp. 1907–1916.
- [8] Mazallon, J., Dai, Z., and Faeth, G. M., 1999, "Primary Breakup of Nonturbulent Round Liquid Jets in Gas Crossflows," *Atomization Sprays*, **9**(3), pp. 291–311.
- [9] Ng, C. L., Sankararishnan, R., and Sallam, K. A., 2008, "Bag Breakup of Nonturbulent Liquid Jets in Crossflow," *Int. J. Multiphase Flow*, **34**(3), pp. 241–259.
- [10] Stenzler, J. N., Lee, J. G., Santavicka, D. A., and Lee, W., 2006, "Penetration of Liquid Jets in a Cross-Flow," *Atomization Sprays*, **16**, pp. 887–906.
- [11] Thawley, S. M., Mondragon, U. M., Brown, C. T., and McDonell, V. G., 2008, "Evaluation of Column Breakpoint and Trajectory for a Plain Liquid Jet Injected Into a Crossflow," *Proceedings of the 21st Annual Conference on Liquid Atomization and Spray Systems*, pp. 1–11.
- [12] Wu, P. K., Kirkendall, K. A., Fuller, R. P., and Nejad, A. S., 1997, "Breakup Processes of Liquid Jets in Subsonic Crossflows," *J. Propul. Power*, **13**(1), pp. 64–73.
- [13] Elshamy, O. M., and Jeng, S. M., 2005, "Study of Liquid Jet in Crossflow at Elevated Ambient Pressures," *Proceedings of the ILASS Americas, 18th Annual Conference on Liquid Atomization and Spray Systems*, pp. 1–10.
- [14] Elshamy, O. M., 2007, "Experimental Investigations of Steady and Dynamic Behavior of Transverse Liquid Jets," Ph.D. thesis, University of Cincinnati.
- [15] Leong, M. Y., McDonell, V. G., and Samuelsen, G. S., 2001, "Effect of Ambient Pressure on an Airblast Spray Injected Into a Crossflow," *J. Propul. Power*, **17**(5), pp. 1076–1084.
- [16] Becker, J., and Hassa, C., 2002, "Breakup and Atomization of a Kerosene Jet in Crossflow at Elevated Pressure," *Atomization Sprays*, **12**, pp. 49–67.
- [17] Herrmann, M., 2008, "A Balanced Force Refined Level Set Grid Method for Two-Phase Flows on Unstructured Flow Solver Grids," *J. Comput. Phys.*, **227**(4), pp. 2674–2706.
- [18] Herrmann, M., 2010, "Detailed Numerical Simulations of the Primary Atomization of a Turbulent Liquid Jet in Crossflow," *ASME J. Eng. Gas Turbines Power*, **132**(6), p. 061506.
- [19] Herrmann, M., 2010, "A Parallel Eulerian Interface Tracking/Lagrangian Point Particle Multi-Scale Coupling Procedure," *J. Comput. Phys.*, **229**, pp. 745–759.
- [20] Herrmann, M., 2009, "Detailed Numerical Simulations of the Primary Atomization of a Turbulent Liquid Jet in Crossflow," *ASME Paper No. GT2009-59563*.
- [21] Herrmann, M., and Gorokhovski, M., 2009, "A Large Eddy Simulation Sub-grid Model for Turbulent Phase Interface Dynamics," *Proceedings of the ICLASS 2009, 11th Triennial International Annual Conference on Liquid Atomization and Spray Systems*, Paper No. ICLASS2009-205.
- [22] Francois, M. M., Cummins, S. J., Dendy, E. D., Kothe, D. B., Sicilian, J. M., and Williams, M. W., 2006, "A Balanced-Force Algorithm for Continuous and Sharp Interfacial Surface Tension Models Within a Volume Tracking Framework," *J. Comput. Phys.*, **213**, pp. 141–173.
- [23] Brackbill, J. U., Kothe, D. B., and Zemach, C., 1992, "A Continuum Method for Modeling Surface Tension," *J. Comput. Phys.*, **100**, pp. 335–354.
- [24] Apte, S. V., Gorokhovski, M., and Moin, P., 2003, "LES of Atomizing Spray With Stochastic Modeling of Secondary Breakup," *Int. J. Multiphase Flow*, **29**(9), pp. 1503–1522.
- [25] Moin, P., and Apte, S. V., 2006, "Large-Eddy Simulation of Realistic Gas Turbine Combustors," *AIAA J.*, **44**(4), pp. 698–708.
- [26] Jiang, G.-S., and Peng, D., 2000, "Weighted ENO Schemes for Hamilton-Jacobi Equations," *SIAM J. Sci. Comput. (USA)*, **21**(6), pp. 2126–2143.
- [27] Shu, C. W., 1988, "Total-Variation-Diminishing Time Discretization," *SIAM (Soc. Ind. Appl. Math.) J. Sci. Stat. Comput.*, **9**(6), pp. 1073–1084.
- [28] Alonso, J. J., Hahn, S., Ham, F., Herrmann, M., Iaccarino, G., Kalitzin, G., LeGresley, P., Mattsson, K., Medic, G., Moin, P., Pitsch, H., Schluter, J., Svard, M., der Weide, E. V., You, D., and Wu, X., 2006, "CHIMPS: A High-Performance Scalable Module for Multi-Physics Simulation," *Proceedings of the 42nd AIAA/ASME/SAE/ASEE Joint Propulsion Conference and Exhibit*, AIAA Paper No. 2006-5274.
- [29] Herrmann, M., and Hajiloo, S., 2008, "Final Report Phase I Option: SBIR Topic N07-046: Advanced Liquid Surface Tracking Software for Predicting Atomization in Gas Turbine Combustors and Augmentors," Technical Report, CASCADE Technologies Inc.

- [30] Stenzler, J. N., Lee, J. G., and Santavicca, D. A., 2003, "Penetration of Liquid Jets in a Cross-Flow," *Proceedings of the 41st Aerospace Sciences Meeting and Exhibit*, Paper No. AIAA 2003-1327.
- [31] Oberlack, M., Wenzel, H., and Peters, N., 2001, "On Symmetries and Averaging of the G-Equation for Premixed Combustion," *Combust. Theory Modell.*, **5**, pp. 363–383.
- [32] Herrmann, M., 2005, "DNS of Turbulent Primary Atomization Using a Level Set/Vortex Sheet Method," *Proceedings of the ILASS Americas 18th Annual Conference on Liquid Atomization and Spray Systems*, Irvine, CA.
- [33] Sallam, K. A., Aalburg, C., and Faeth, G. M., 2004, "Breakup of Round Nonturbulent Liquid Jets in Gaseous Crossflow," *AIAA J.*, **42**(12), pp. 2529–2540.
- [34] Sirovich, L., 1987, "Turbulence and the Dynamics of Coherent Structures," *Q. Appl. Math.*, **42**, pp. 561–590.
- [35] Arienti, M., and Soteriou, M. C., 2009, "Time-Resolved Proper Orthogonal Decomposition of Liquid Jet Dynamics," *Phys. Fluids*, **21**(112104), pp. 1–15.
- [36] Villermaux, E., 1998, "Mixing and Spray Formation in Coaxial Jets," *J. Propul. Power*, **14**(5), pp. 807–817.
- [37] Yecko, P., Zaleski, S., and Fullana, J.-M., 2002, "Viscous Modes in Two-Phase Mixing Layers," *Phys. Fluids*, **14**(12), pp. 4115–4122.
- [38] Boeck, T., and Zaleski, S., 2005, "Viscous vs Inviscid Instability of Two-Phase Mixing Layers With Continuous Velocity Profile," *Phys. Fluids*, **17**(3), p. 032106.